


Electron metasurfaces in graphene

Ruihuang Zhao¹, Pengcheng Wan, Ling Zhou, Di Huang, Haiqin Guo, Hao Xia, and Junjie Du^{1*}
*State Key Laboratory of Precision Spectroscopy, School of Physics and Electronic Science,
 East China Normal University, Shanghai 200062, China*

 (Received 28 October 2021; revised 20 February 2023; accepted 21 March 2023; published 6 April 2023)

For electron optics in graphene, the propagation effect has so far been the only physical mechanism available. The resulting optics-inspired electronic components are large in size and operate at low temperatures to avoid violating the ballistic transport limits. Here, electron metasurfaces, i.e., electronic counterparts of optical metasurfaces, are introduced for graphene electronics. We theoretically implement various angles of electron beam bending, as well as beam splitting at corresponding angles in the same metasurface with the functionalities switched freely by controlling the applied gate biases. The wavefront of electron beams is shaped within a distance far below the ballistic transport distance at room temperature, allowing for the realization of optics-inspired electronic devices that can operate under ambient conditions. The concept of metasurface electron optics, based on elaborate design of more complex spatial phase patterns, might also open up a promising avenue for achieving more appealing applications such as electron metalenses, metasurface holography, as well as metasurface-based digital coding technology in graphene.

DOI: [10.1103/PhysRevB.107.155404](https://doi.org/10.1103/PhysRevB.107.155404)

I. INTRODUCTION

Low-energy graphene electrons behave like light because of their lightlike dispersion and the ballistic transport [1]. Electron optics in semiconductor structures can be naturally extended to graphene. Both naturally occurring and non-naturally occurring optical phenomena, such as the Goos-Hanchen shift [2], self-collimation [3], whispering-gallery modes [4–8], and negative-index [9–12] and zero-index [13] behaviors, have been reproduced by graphene electrons. Accordingly, various optics-inspired functional units, such as two-dimensional electron microscopes [14,15], quantum switches [16–18], Fabry-Pérot cavities [19], electron waveguides [20–22], splitters [23,24], and Veselago lenses [10–12], have been demonstrated. However, these remarkable achievements were made by following procedures used for bulk optical materials where wavefront shaping is accomplished via light propagation over a distance much larger than the wavelength. The propagation effect dictates that the optics-inspired electronic components are large in size. But, even if the large size of the devices can be tolerated, the required long propagation distances often challenge the ballistic transport limits. To avoid violating these ballistic transport limits, these components have been designed to operate at low temperature since the mean free path of graphene electrons, $l = \mu\sqrt{\rho/\pi}h/2e$, which determines the ballistic transport limit, becomes larger at low temperature with enhanced carrier mobility μ [25].

The emergence of optical metasurfaces [26,27] and metagratings [28,29] opens the door to flat optics technology characterized by a single layer of nanoparticles. Wavefront

shaping in optical metasurfaces is achieved over the scale of the free-space wavelength or on a smaller scale by introducing abrupt changes in phase or amplitude, following the generalized Snell's law [26,30]. This is fundamentally different from conventional diffractive optics based on the propagation effect. While metasurfaces greatly shrink the size of devices and simplify the fabrication process in contrast to bulk materials, they can also mould optical wavefronts into shapes that are designed at will [30]. Inspired by the compactness features and the remarkable capabilities of wavefront engineering, we explore the possibility of realizing electron metasurfaces for electrons in graphene. As will be demonstrated, electron metasurfaces are usually only a few nanometers thick, far smaller than the ballistic transport distance (about $1\ \mu\text{m}$) of graphene electrons at room temperature. As a result, electron metasurfaces break the dimensional limit of optics-inspired electronic devices and enable them to operate under ambient conditions. Also worth noting is that Dirac fermion metagratings with the same compactness have been demonstrated in graphene [31]. However, incident electron waves are only channeled into the direction of a specific diffracted order supported by metagratings. As a comparison, an arbitrary channel direction is obtainable in metasurfaces by engineering the phase gradient along the interfaces. This has led to the realization of spherical-aberration-free, high numerical aperture optical flat lenses [32]. Moreover, hologram metasurfaces and programmable coding metasurfaces have brought about unprecedented opportunities for the improvement of holography [33,34] and optical information technologies [35,36]. The same opportunities could be brought to graphene electron systems via electron metasurfaces. In addition to the inherent advantages of metasurfaces such as compactness, low loss, and easy fabrication, we will show that electron metasurfaces are exceptional in many other aspects such as perfect

*phyjunjie@gmail.com

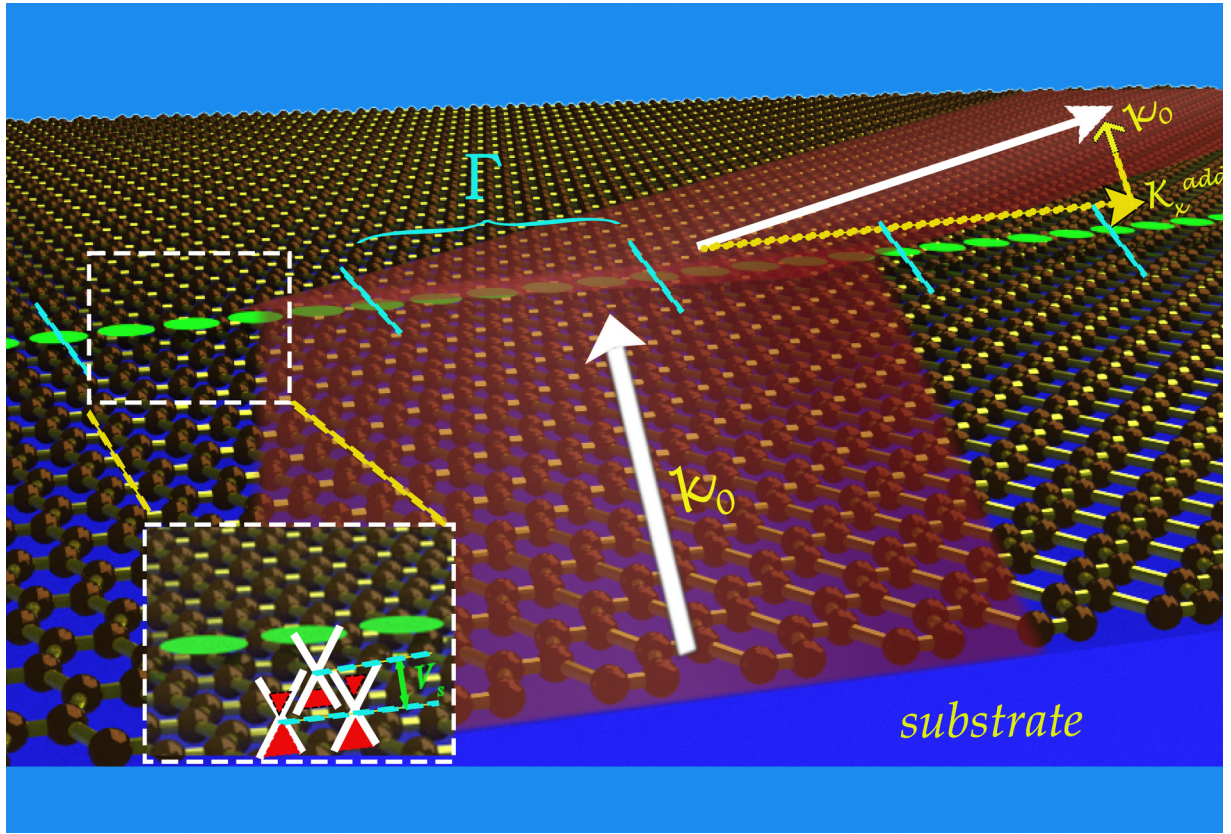


FIG. 1. Schematic view of the bending of electron beams by a metasurface realized by a one-dimensional array of QDs with the spacing between QDs d on graphene. The m_{unit} QDs with linear increasing bias V_s applied constitute a unit cell of the metasurface with unit cell length (or the period of the metasurface is) $\Gamma = (m_{\text{unit}} - 1)d$. Phase shifts in one unit cell cover the 0 to 2π range to realize the full control of the wavefront. QDs are denoted by the green circular regions and the m_{unit} is set to 6 in the diagram.

operating efficiency and high tunability, which are not even expected in optical metasurfaces.

II. RESULTS AND DISCUSSION

Formally, an electron metasurface is a linear array of gate-bias-controlled circular quantum dots (QDs), as shown schematically in Fig. 1 where the green circular regions represent QDs. The scattering electron waves off of each QD differ in phase so as to construct a constant gradient of phase jump in metasurfaces. For the sake of understanding, we analogize the QDs with optical systems and can think that the QD phase response is related to their “refractive index,” which is defined as $n_s = (E - V_s)/E$, where E is the incident energy and V_s the applied bias [37]. The dependence of n_s on V_s allows the same QDs to exhibit a different phase response by controlling the applied bias voltages V_s and enables the design of unit cells of metasurfaces with the same QDs. The unit cells consist of m_{unit} QDs and their length $\Gamma = (m_{\text{unit}} - 1)d$ is the period of the metasurface. A unit cell usually covers the entire 0 - 2π range and thus introduces a lateral wave number $k_x^{\text{add}} = d\Phi/dx = 2\pi/\Gamma$ because of the gradient change of the phase response between QDs.

The low-energy electron dynamics can be described by the single-valley Dirac-Hamiltonian [37–43],

$$H = -i\hbar v_F \nabla \sigma + V_s \Theta(R_s - r), \quad (1)$$

in the presence of circular QDs whose potentials are smooth on the scale of the graphene’s intrinsic lattice constant, but sharp on the scale of the de Broglie wavelength. Here, R_s is the radius of QDs and the potential is described by the Heaviside step function $\Theta(R_s - r)$, which is an approximation to the gradual transition of potentials. In practice, it has been shown that the electron scattering behavior of QDs remains nearly the same [44] when the transition distance is less than $0.5R_s$. For the Hamiltonian in Eq. (1), the conserved quantity is the pseudo-angular momentum operator $\hat{j} = \hat{l} + \frac{1}{2}\sigma_z$ with the eigenvalue $j = m + \frac{1}{2}$ (see the Appendices). The corresponding eigenvector is

$$\psi_m = \begin{pmatrix} -ih_j^{(1)}(k_0 r) e^{in\phi} \\ \alpha h_{j+1}^{(1)}(k_0 r) e^{i(n+1)\phi} \end{pmatrix} \propto \begin{pmatrix} -iH_m^{(1)}(k_0 r) e^{in\phi} \\ \alpha H_{m+1}^{(1)}(k_0 r) e^{i(n+1)\phi} \end{pmatrix}, \quad (2)$$

where $m = 0, \pm 1, \pm 2, \dots$, $h_n^{(1)}$ and $H_n^{(1)}$ are the n th-order spherical and cylindrical Hankel function of the first kind. With the help of the complete spherical wave basis, the Mie scattering method used widely in optics is applicable to the electron scattering problem by such QDs [37–43] (see the Appendices). Many important results have been predicted by the method, some of which have been verified in experiment [45–49].

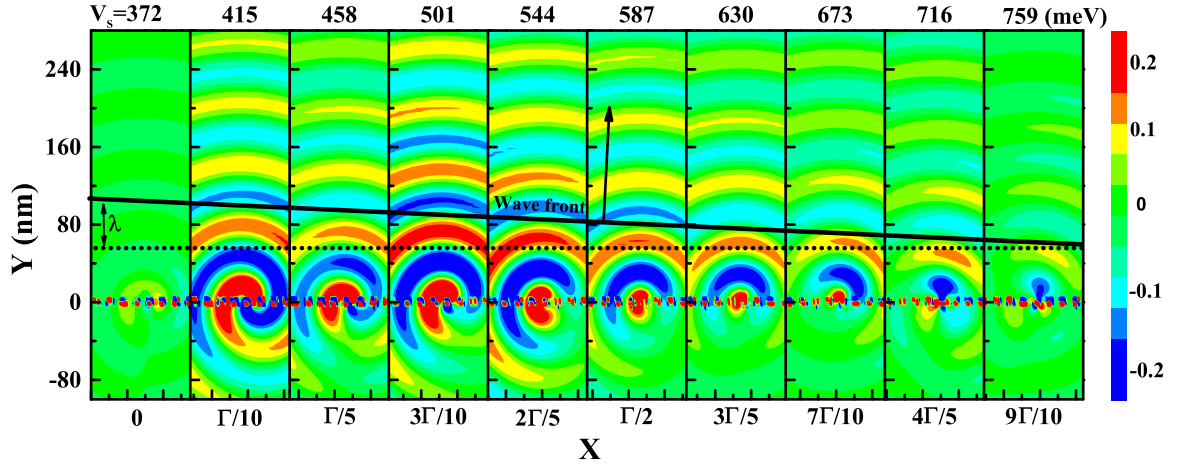


FIG. 2. The scattering field of the individual QDs constituting the unit cell of a metasurface. The tilted black straight line is the envelope of the projections of the cylindrical waves scattered by the QDs. A complete phase coverage from 0 to 2π is shown with an approximately constant phase difference $\Delta\phi = \pi/5$ between neighbors. The number of QDs in the unit cell is $m_{\text{unit}} = 10$ and the biases V_s applied on each QD are given above each plot. The inter-QD coupling interaction has been considered in this calculation.

As is well known, the behavior of a wave in a metasurface follows the generalized Snell's law of refraction [26],

$$n_t \sin \theta_t - n_i \sin \theta_i = \frac{1}{k_0} \frac{d\Phi}{dx}, \quad (3)$$

where k_0 is the magnitude of the free-space wave vector, θ_i and θ_t are, respectively, the angle of incidence and refraction, and n_i and n_t are the respective “refractive indices” of media on the incident and transmission sides of the metasurface. The phase gradient $d\Phi/dx$ implies an effective wave vector (equivalently, an effective momentum) along the interface that is produced and is imparted to the transmitted and reflected electrons. Thus the transmitted and reflected electron beams can be deflected through arbitrary angles, depending on the direction and magnitude of the phase gradient. The phase gradient is created within a unit cell consisting of several QDs to which the linearly increasing biases V_s are respectively applied. The variation of bias indicates the difference in refractive index between the QDs and thus the difference in the phase response of the electron waves. Figure 2 illustrates a linear phase distribution of the scattering fields in a unit cell composed of 10 QDs. Throughout this paper, the energy of the incident electron beams with waist radius $w = 240$ nm is chosen to be $E = 65.82$ meV and the radius of the QDs to be 5 nm, with a spacing $d = 14.6$ nm between them. So the period of the metasurface in Fig. 2 is $\Gamma = 9d = 131.4$ nm; in this figure, the biases are given above each scattering field plot. Highly collimated electron beams with angular width 18° or narrower have been experimentally achieved in graphene by using collinear pairs of slits with absorptive sidewalls between the slits [15]. Figure 2 shows that a complete phase coverage from 0 to 2π is obtained with an approximately constant phase difference $\Delta\phi = \pi/5$ between neighbors. Thus the magnitude of the introduced wave vector in the x direction is $k_x^{\text{add}} = d\Phi/dx = 2\pi/\Gamma = 0.048/\text{nm}$. When a normal-incidence electron beam impinges on the metasurface, the transmitted beam will be bent at an angle $\theta_{\text{calc}} = \arctan(k_x^{\text{add}}/k_0)$, where k_0 is the magnitude of the free-space wave vector with $n_i = n_t = 1$. This is simulated

in Fig. 3(a), and the travel direction of the transmitted beam agrees well with the calculated bending angle, $\theta_{\text{calc}} = 25^\circ$. Note that the scattering field of each QD in Fig. 2 is calculated by considering the inter-QD coupling interaction and employing multiple scattering theory [31,50,51]. This ensures that the constant gradient of the phase jumps really exists in the metasurface since the scattering field of an isolated QD may be very different from that of the same QD in a linear array. The bending angle can be altered by adjusting the spacing d with a slight change of bias.

A unit cell which covers the entire $0-2\pi$ range can also be composed of different numbers of QDs by adjusting only the bias while keeping the array invariant. We denote the number of the QDs in a unit cell by m_{unit} . A decrease of m_{unit} implies a larger phase gradient and also a larger introduced wave vector and a larger bending angle. Figures 3(b)–3(f) show the bending of the electron beams by metasurfaces with $m_{\text{unit}} = 9, 8, 7, 6,$ and 5 . The bending angle increases gradually from Fig. 3(b) to Fig. 3(f). In addition, the Dirac fermion metasurfaces show a remarkable property in Fig. 3, i.e., electron waves can be bent with nearly perfect efficiency, especially for bending angles below 45° . This is strikingly different from optical metasurfaces, in which an efficiency near 100% is difficult to achieve. It shows that electrons can more easily react to the lateral momentum introduced by the phase gradient than can photons. Moreover, comparing the panels in Fig. 3 shows that the efficiency is closer to 100% in the case of the longer unit cells because electrons have more opportunities to react to the introduced lateral momentum. Finally, perfect efficiency cannot be divorced from the successful suppression of reflection in the metasurfaces (see Fig. S2 in the Supplemental Material [52]).

To verify that the beam bending at various θ_{actu} in Fig. 3 can be well explained by the introduced wave vectors due to phase gradient, we made a comparison between the two for all the cases in Table I where $\tan \theta_{\text{calc}} = k_x^{\text{add}}/k_0$ and $\tan \theta_{\text{actu}}$ are given. Here, $k_x^{\text{add}} = 2\pi/\Gamma = 2\pi/m_{\text{unit}}d$ and θ_{actu} is directly read from Fig. 3. The calculated bending angles agree well with the actual ones for m_{unit} between 7 and 10, but there are

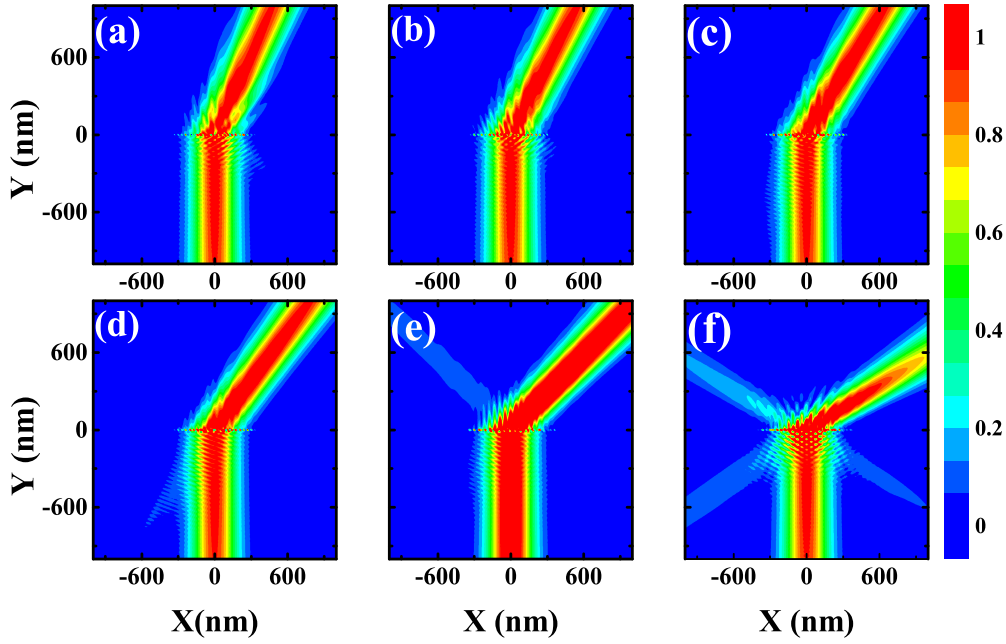


FIG. 3. The bending of electron beams after passing through the metasurface composed of unit cells with the number of QDs m_{unit} equal to (a) 10, (b) 9, (c) 8, (d) 7, (e) 6, and (f) 5. Linearly increasing biases with constant gradient are applied to the QDs in the unit cells. They are, respectively, $V_s = 375, 420, 465, 510, 555, 600, 645, 690,$ and 735 meV for $m_{\text{unit}} = 9$; $V_s = 385, 440, 495, 550, 605, 660, 715,$ and 770 meV for $m_{\text{unit}} = 8$; $V_s = 385, 440, 495, 550, 605, 660,$ and 715 meV for $m_{\text{unit}} = 7$; $V_s = 400, 470, 540, 610, 680,$ and 750 meV for $m_{\text{unit}} = 6$; and $V_s = 390, 450, 510, 570,$ and 630 meV for $m_{\text{unit}} = 5$.

distinct deviations for $m_{\text{unit}} = 6$ and 5. To make matters worse, a weak beam is transmitted to the left of the normal in the latter two cases. In an effort to find the causes of these deviations, we examine the phase response of each quantum dot for the case of $m_{\text{unit}} = 6$, as shown in Fig. 4(a). One can see that only the former five QDs contribute to the formation of the linear phase gradient, whereas the QD with $V_s = 750$ meV has a phase that goes against the linear gradient change. Moreover, this QD and the next two QDs of $V_s = 680$ meV and $V_s = 400$ meV together form a phase gradient increasing in the opposite direction; hence, a left-oriented wave vector is produced, as shown in Fig. 4(a). Thus a small portion of electrons will propagate on the left side of the normal in Fig. 3(e). Accordingly, the magnitude of the introduced right-oriented wave number should be calculated in terms of the period $\Gamma' = 4d = 58.4$ nm. The new $\tan \theta_{\text{calc}}$ calculated by $k_x^{\text{add}} = 2\pi/\Gamma'$ is equal to 1.075 and agrees well with $\tan \theta_{\text{actu}}$ in Table I. Similarly, the deviation in the case of $m_{\text{unit}} = 5$ in Table I has the same cause (see Fig. S1 in the Supplemental Material [52]).

Exploring the causes of deviations can help to improve the efficiency of metasurfaces. We note that the electron scattering of the QD of $V_s = 750$ meV is weak in contrast to other QDs

in the unit cell. So the scattering of the other QDs will hardly be impacted if this QD is removed from the unit cell. Such a unit cell is schematically shown in the lower panel in Fig. 4(b) and the phase distribution is given in Fig. 4(c). We see that the opposite phase gradient is eliminated and thus only a right-oriented wave vector is introduced. The electron density distribution displayed in Fig. 4(d) shows that the electron beam bends to the right side of the normal with near-unit efficiency when the QD of $V_s = 750$ meV is removed.

Since two equal and oppositely directed phase gradients represent left- and right-oriented equal-magnitude wave vectors, we can introduce them simultaneously in a metasurface to design an ultrathin electron splitter. One simple route for splitters is to achieve a right-oriented wave vector by the unit cells in the right half of the array and a left-oriented wave vector by the unit cells in the left half. This can be implemented by applying the biases enhanced from left to right to the QDs in the unit cells in the right half, as shown in Fig. 3, and the same biases but enhanced in the opposite direction in the left half. The impinging beam is split into two sub-beams at various angles to each other, as demonstrated in Figs. 5(a)–5(f). We see that the beams are split with nearly perfect efficiency again and the splitting ratio is 50-50 in all cases.

Three points are worth emphasizing in the model. First of all, all the results reported in this paper are obtained in the same linear array of QDs. Specifically, the radius of the QDs and the spacing between them remain invariant in all simulations and we only modulate the biases on the QDs to realize both beam bending and beam splitting at various angles. The fast switching time of bias systems allows for high modulation efficiency. Second, near-perfect efficiency is obtainable,

TABLE I. Comparison between the calculated and actual bending angles for various m_{unit} .

m_{unit}	10	9	8	7	6	5
$\tan \theta_{\text{calc}}$	0.480	0.535	0.600	0.715	0.861	1.074
$\tan \theta_{\text{actu}}$	0.468	0.526	0.620	0.760	1.000	1.700

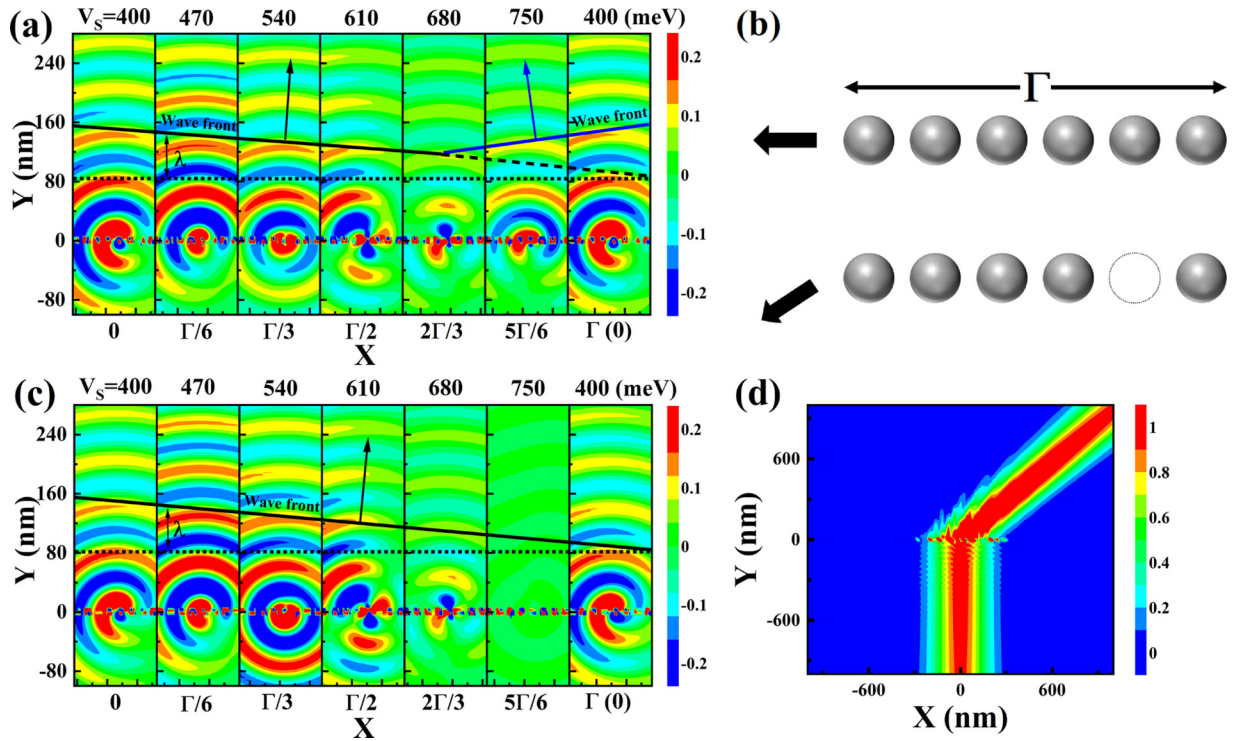


FIG. 4. (a) The scattered field of the individual QDs in the presence of all six QDs. The tilted black and blue solid lines indicate, respectively, the desired and undesired phase gradients formed in the unit cell. (b) Schematics of the unit cells in the presence of all the QDs in the upper panel and in the absence of the QD of $V_s = 750$ meV in the lower panel. (c) The scattered field of the individual QDs with the QD of $V_s = 750$ meV removed. The phase gradient increasing in the opposite direction that appears in (a) is eliminated. (d) The beam bending occurring with near-unit efficiency when the QD of $V_s = 750$ meV is removed, in sharp contrast to Fig. 3(e).

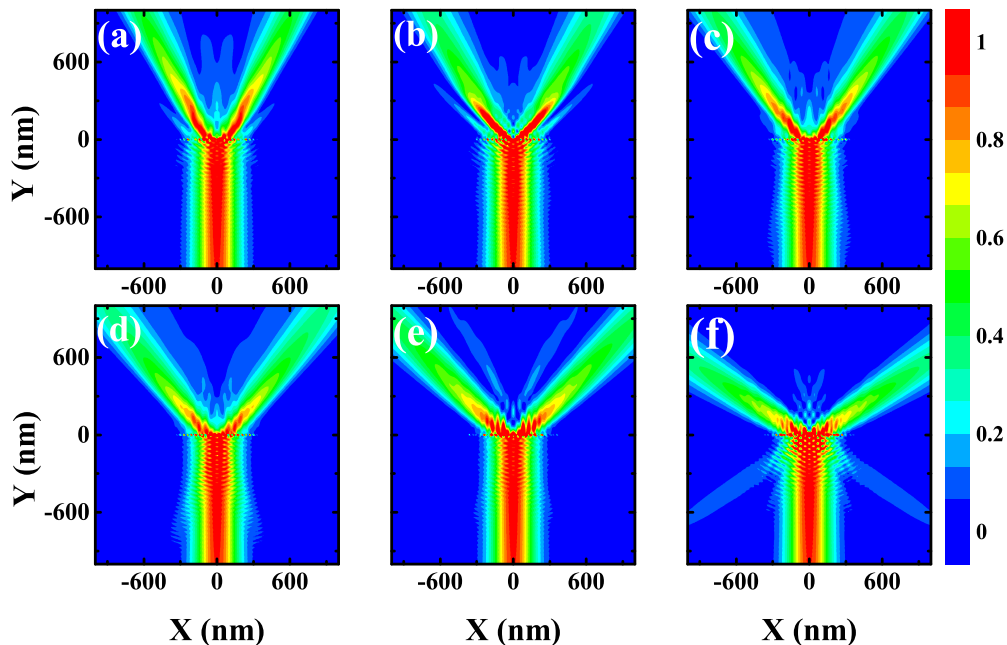


FIG. 5. The splitting of electron beams after passing through a metasurface composed of unit cells with the number of QDs m_{unit} equal to (a) 10, (b) 9, (c) 8, (d) 7, (e) 6, and (f) 5. The unit cells in the right half of the metasurfaces in (a)–(f) are the same as those in Figs. 3(a)–3(f), respectively, whereas the unit cells in the left half have the biases increasing in the opposite direction.

which is fundamentally different from optical counterparts. The performance of optical metasurfaces is subject to the intrinsic nature of light. The introduced momentum through the phase gradient cannot be perceived by all the photons due to the absence of interaction between photons. Because electrons are distinct from photons, the electron metasurfaces have near-perfect operating efficiency. Third, the 5-nm radius QDs used in our simulations fall within current experimental manufacturing tolerance. Very recently, even smaller circular QDs with atomically sharp boundaries have been obtained by substrate engineering in experiment [46–48]. QDs can also be created by positioning a charged scanning tunneling microscopy (STM) tip above graphene [49] or by some chemical approaches [53]. The fabrication techniques of high-precision QDs and the tunability of bias V_s applied on them makes experimental realization of the metasurfaces feasible. Finally, it is worth noting that the electron metasurfaces in graphene that we are studying are extremely different from “graphene metasurfaces.” The latter refers to a class of optical metasurfaces made from graphene.

III. CONCLUSION

In summary, we have demonstrated theoretically the feasibility of realizing metasurfaces for graphene ballistic electrons. A simple metasurface is a linear array of quantum dots (QDs) of the same radius. Phase discontinuities, the essential ingredient of gradient metasurfaces, are acquired by applying difference biases to the QDs. Following the generalized Snell’s law, the metasurface imposes a control over electrons in a rather compact way, with wavefront shaping accomplished below the ballistic transport limit at room temperature. Such metasurfaces dramatically reduce the size of electron-optics-based components and enable them to get rid of the dependence on low-temperature conditions. The two kinds of transistors we demonstrated, beam benders and beam splitters, are achieved in the same linear array of QDs and can be conveniently switched back and forth by tuning the biases applied to the QDs. Electron metasurfaces represent a promising way to develop more practical and accessible electron optics technologies.

APPENDIX A: THE SPHERICAL WAVE BASIS OF EIGENSTATES OF THE SINGLE-VALLEY DIRAC HAMILTONIAN

The problem we consider in this paper only deals with the dynamics on the scale much larger than the graphene’s intrinsic lattice constant and intervalley scattering can therefore be neglected. Thus, the low-energy electron dynamics is described by the single-valley Dirac-Hamiltonian [37,42],

$$H_0 = -i\hbar v_F \nabla \sigma. \quad (\text{A1})$$

We first consider the eigenproblem of the Hamiltonian

$$H_0 \psi = \epsilon \psi, \quad (\text{A2})$$

where ψ is the two-component spinor,

$$\psi(\mathbf{r}) = \begin{pmatrix} \varphi \\ \chi \end{pmatrix}. \quad (\text{A3})$$

In the plane-wave basis, the expression of $\psi(\mathbf{r})$ is $\psi(\mathbf{r}) = \begin{pmatrix} A \\ B \end{pmatrix} e^{i\mathbf{k}\cdot\mathbf{r}}$. Substituting it into (A2), one obtains the relativistic dispersion $\epsilon = \alpha \hbar k v_F$, where $\alpha = \pm 1$ distinguishes between the particle and hole sectors. It follows that

$$\psi(\mathbf{r}) = \frac{1}{\sqrt{2}} \begin{pmatrix} e^{-i\frac{\varphi_k}{2}} \\ \alpha e^{i\frac{\varphi_k}{2}} \end{pmatrix} \quad (\text{A4})$$

from $\psi^\dagger(\mathbf{r})\psi(\mathbf{r}) = 1$, with φ_k the incident angle.

To develop the scattering theory of circular gate-controlled quantum dots, we need to express the eigenstates in the spherical wave basis. This can be done based on the fact that for a rotational symmetric potential, the pseudo-angular momentum operator is the conserved quantity, i.e., $[\hat{j}_z, H] = 0$, where $\hat{j}_z + \frac{1}{2}\sigma_z$. Another conserved quantity is the parity of the states which requires that the spinor components transform as $\varphi(-\mathbf{r}) = \varphi(\mathbf{r})$ and $\chi(-\mathbf{r}) = -\chi(\mathbf{r})$ under inversion $\mathbf{r} \rightarrow -\mathbf{r}$ (i.e., $\varphi \rightarrow \varphi + \pi$). We know that the angular parts of φ and χ are of the $e^{im\varphi}$ form, similar to the two-dimensional (2D) nonrelativistic scalar particle. Under the conservation of parity, the angular parts of φ and χ correspond to $l_z = m$ and $l_z = m + 1$, respectively, so that the m component of ψ has the definite parity $(-1)^m$. Thus, ψ_m with fixed projection $m = 0, \pm 1, \pm 2, \dots$, of angular momentum on the z axis, can be expressed as

$$\psi_m(\mathbf{r}) = \begin{pmatrix} -iF_m(r)e^{im\varphi} \\ G_m(r)e^{i(m+1)\varphi} \end{pmatrix}. \quad (\text{A5})$$

Substituting it into the eigenequation, we obtain the differential equations that the radial functions $F_m(r)$ and $G_m(r)$ satisfy:

$$-\frac{1}{r} \frac{d}{dr} \left(r \frac{dF_m}{dr} \right) + \frac{m^2}{r^2} F_m = k^2 F_m, \quad (\text{A6})$$

$$-\frac{1}{r} \frac{d}{dr} \left(r \frac{dG_m}{dr} \right) + \frac{(m+1)^2}{r^2} G_m = k^2 G_m. \quad (\text{A7})$$

They can be reduced to the Bessel equations that have two linear independent solutions, i.e., cylindrical Bessel function and Hankel function of the first/second kind (or Neumann function N_m). Though the spherical wave basis of the eigenstates is the intended result, the final radial wave function is the cylindrical Bessel functions. This is because the conserved quantity is the pseudo-angular momentum operator with the eigenvalue $j = m + \frac{1}{2}$. As a result, the spherical Bessel functions $j_m(kr)$ are transformed into the cylindrical Bessel functions $J_m(kr)$. The Bessel function J_m and J_{m+1} should be, respectively, chosen for $F_m(r)$ and $G_m(r)$ regular at the origin. Once $F_m(r)$ and $G_m(r)$ are known, $\psi_m(\mathbf{r})$ in (A5) is completely given. For more details, please refer to Ref. [41].

These $\psi_m(\mathbf{r})(m = 0, \pm 1, \pm 2, \dots)$ constitute a complete spherical wave basis by which the Mie scattering method can be developed to solve the electron scattering problem by a circular potential.

APPENDIX B: MIE SCATTERING METHOD AND MULTIPLE SCATTERING METHOD

For an incident plane wave, it can be expanded in the spherical wave basis as

$$\psi_{in} = \frac{1}{\sqrt{2}} \sum_{m=-\infty}^{+\infty} i^{m+1} \begin{pmatrix} -i p_m^A J_m(k_0 r) e^{im\phi} \\ \alpha p_m^B J_{m+1}(k_0 r) e^{i(m+1)\phi} \end{pmatrix}, \quad (\text{B1})$$

by substituting the decomposition of the plane wave,

$$e^{i\mathbf{k}\cdot\mathbf{r}} = \sum_{n=-\infty}^{+\infty} i^n e^{i\varphi_n} J_n(kr) e^{in\varphi}, \quad (\text{B2})$$

into (A4). Here, $p_m^A = e^{-i(m+\frac{1}{2})\varphi_k}$ and $p_m^B = e^{-i(m-\frac{1}{2})\varphi_k}$, with φ_k the incident angle. (B1) is equally applicable to an incident Gaussian beam and the difference from a plane incident wave is only p_m^A and p_m^B .

We consider elastic electron scattering off a circular gate-controlled quantum dot of radius R_s whose potential is described by the Heaviside step function $V_s \Theta(R_s - r)$. The Hamiltonian is

$$H_0 = -i\hbar v_F \nabla_\sigma + V_s \Theta(R_s - r). \quad (\text{B3})$$

The Mie scattering method now can be developed to solve the electron scattering problem of a single gate-controlled quantum dot (QD) in graphene [37–44] by expanding the scattering waves and the inner waves using (B2). The scattered waves are written as

$$\psi_s = \frac{1}{\sqrt{2}} \sum_{m=-\infty}^{+\infty} a_m i^{m+1} \begin{pmatrix} -i H_m^{(1)}(k_0 r) e^{im\phi} \\ \alpha H_{m+1}^{(1)}(k_0 r) e^{i(m+1)\phi} \end{pmatrix}, \quad (\text{B4})$$

when F_m and G_m are selected as Hankel functions of the first kind. The inner field inside the dot can be written as

$$\psi^{ins} = \frac{1}{\sqrt{2}} \sum_{m=-\infty}^{+\infty} d_m i^{m+1} \begin{pmatrix} -i J_m(k_s r) e^{im\phi} \\ \alpha' J_{m+1}(k_s r) e^{i(m+1)\phi} \end{pmatrix}, \quad (\text{B5})$$

where Bessel functions are used to guarantee that the spinor wave is regular at the origin. Here, k_0 and k_s are, respectively, the wave vector in the background region and the QD, the index $\alpha = 1$ represents the conduction band, $\alpha' = -1$ represents the valence band, and $k_s = n_s k_0$ with the refractive index $n_s = \frac{E - V_s}{E}$. After imposing the boundary condition at the surface of the QD with its radius R_s , the size parameter

$\rho = k_0 R_s$ is introduced and the scattering coefficient a_m is given,

$$a_m = -\frac{J_m(\rho) J_{m+1}(N\rho) p_m^A - \alpha \alpha' J_{m+1}(\rho) J_m(N\rho) p_m^B}{J_{m+1}(N\rho) H_m^{(1)}(\rho) - \alpha \alpha' J_m(N\rho) H_{m+1}^{(1)}(\rho)}, \quad (\text{B6})$$

$$a_{-m} = -\frac{J_m(\rho) J_{m-1}(N\rho) p_{-m}^A - \alpha \alpha' J_{m-1}(\rho) J_m(N\rho) p_{-m}^B}{J_{m-1}(N\rho) H_m^{(1)}(\rho) - \alpha \alpha' J_m(N\rho) H_{m-1}^{(1)}(\rho)}. \quad (\text{B7})$$

The relation between the scattering coefficients a and the incident coefficients (p_{β}^A) in (B6) and (B7) can also be expressed as $a = S p$ by a scattering matrix S .

In a linear QD array, the incident wave that strikes the surface of QD j consists of two parts: (1) the initial incident wave $\psi_{inc}^0(j)$ and (2) the scattered waves of all other QDs according to multiple scattering theory [50,51] (also known in solid-state physics as the K.K.R. method [54,55]). Thus it can be written as

$$\psi_{inc}(j) = \psi_{inc}^0(j) + \sum_{l \neq j} \psi_s(l). \quad (\text{B8})$$

By the translational addition theorem, the scattered wave from any other potential l (with $l \neq j$) can be expanded as follows:

$$\psi_s(l) = \frac{1}{\sqrt{2}} \sum_{n=-\infty}^{+\infty} a_n^{(l)} i^{n+1} \begin{pmatrix} -i H_n^{(1)}(k_0 r) e^{in\phi} \\ \alpha H_{n+1}^{(1)}(k_0 r) e^{i(n+1)\phi} \end{pmatrix}$$

$$= \frac{1}{\sqrt{2}} \sum_{m=-\infty}^{+\infty} i^{m+1} \begin{pmatrix} -i p_m^{(l,j)} J_m(k_0 r) e^{im\phi} \\ \alpha p_m^{(l,j)} J_{m+1}(k_0 r) e^{i(m+1)\phi} \end{pmatrix}, \quad (\text{B9})$$

where

$$p_m^{(l,j)} = \sum_n i^{(m-n)} H_{m-n}^{(1)}(k d_{lj}) e^{-i(m-n)\phi_{lj}} a_n^{(l)}$$

and $\mathbf{d}_{lj} = d_{lj} \cos \phi_{lj} \hat{e}_x + d_{lj} \sin \phi_{lj} \hat{e}_y$ is the vector extending from the center of QD l to that of QD j . In the main text, the linear QD array is placed along the x axis, so the angle θ_{WA} between the incident wave and the array equals the angle of incidence, ϕ_{inc} .

Substituting (B9) into (B8) and $a^{(j)} = S p^{(j)}$, one will yield a set of linear equations that contains the iterative scattering coefficients. With the equations, we can compute the scattering field at any position. In our practical numerical calculation, the series expansion was truncated at some $n = n_c$, which is chosen such that a further increase in n_c does not change the value of the calculated field.

- [1] A. K. Geim and K. S. Novoselov, The rise of graphene, *Nat. Mater.* **6**, 183 (2007).
- [2] C. W. J. Beenakker, R. A. Sepkhanov, A. R. Akhmerov, and J. Tworzydło, Quantum Goos-Hänchen Effect in Graphene, *Phys. Rev. Lett.* **102**, 146804 (2009).
- [3] C.-H. Park, Y.-W. Son, L. Yang, M. L. Cohen, and S. G. Louie, Electron beam supercollimation in graphene superlattices, *Nano Lett.* **8**, 2920 (2008).
- [4] Y. Zhao, J. Wyrick, F. D. Natterer, J. F. Rodriguez-Nieva, C. Lewandowski, K. Watanabe, T. Taniguchi, L. S. Levitov, N. B. Zhitenev, and J. A. Strosio, Creating and probing

electron whispering-gallery modes in graphene, *Science* **348**, 672 (2015).

- [5] Y. Jiang, J. Mao, D. Moldovan, M. R. Masir, G. Li, K. Watanabe, T. Taniguchi, F. M. Peeters, and E. Y. Andrei, Tuning a circular p-n junction in graphene from quantum confinement to optical guiding, *Nat. Nanotechnol.* **12**, 1045 (2017).
- [6] F. Ghahari, D. Walkup, C. Gutierrez, J. F. Rodriguez-Nieva, Y. Zhao, J. Wyrick, F. D. Natterer *et al.*, An on/off Berry phase switch in circular graphene resonators, *Science* **356**, 845 (2017).
- [7] P. Hewageegana and V. Apalkov, Electron localization in graphene quantum dots, *Phys. Rev. B* **77**, 245426 (2008).

- [8] J. H. Bardarson, M. Titov, and P. W. Brouwer, Electrostatic Confinement of Electrons in an Integrable Graphene Quantum Dot, *Phys. Rev. Lett.* **102**, 226803 (2009).
- [9] V. V. Cheianov, V. Fal'ko, and B. L. Altshuler, The focusing of electron flow and a Veselago lens in graphene pn junctions, *Science* **315**, 1252 (2007).
- [10] S. Chen, Z. Han, M. M. Elahi, K. M. Habib, L. Wang, B. Wen, Y. Gao *et al.*, Electron optics with p-n junctions in ballistic graphene, *Science* **353**, 1522 (2016).
- [11] G.-H. Lee, G.-H. Park, and H. J. Lee, Observation of negative refraction of Dirac fermions in graphene, *Nat. Phys.* **11**, 925 (2015).
- [12] B. Brun, N. Moreau, S. Somanchi, V.-H. Nguyen, K. Watanabe, T. Taniguchi, J.-C. Charlier, C. Stampfer, and B. Hackens, Imaging Dirac fermions flow through a circular Veselago lens, *Phys. Rev. B* **100**, 041401(R) (2019).
- [13] Y. Ren, P. Wan, L. Zhou, R. Zhao, Q. Wang, D. Huang, H. Guo, and J. Du, Zero-index metamaterials for Dirac fermion in graphene, *Phys. Rev. B* **103**, 085431 (2021).
- [14] P. Bøggild, J. M. Caridad, C. Stampfer, G. Calogero, N. R. Papior, and M. Brandbyge, A two-dimensional Dirac fermion microscope, *Nat. Commun.* **8**, 15783 (2017).
- [15] A. W. Barnard, A. Hughes, A. L. Sharpe, K. Watanabe, T. Taniguchi, and D. Goldhaber-Gordon, Absorptive pinhole collimators for ballistic Dirac fermions in graphene, *Nat. Commun.* **8**, 15418 (2017).
- [16] K. Wang, M. M. Elahi, L. Wang, K. M. M. Habib, T. Taniguchi, K. Watanabe, J. Hone, A. W. Ghosh, G.-H. Lee, and P. Kim, Graphene transistor based on tunable dirac fermion optics, *Proc. Natl. Acad. Sci. USA* **116**, 6575 (2019).
- [17] R. N. Sajjad and A. W. Ghosh, High efficiency switching using graphene based electron optics, *Appl. Phys. Lett.* **99**, 123101 (2011).
- [18] Q. Wilmart, S. Berrada, D. Torrin, V. H. Nguyen, G. Fève, J. M. Berroir, P. Dollfus, and B. Plaçais, A Klein-tunneling transistor with ballistic graphene, *2D Mater.* **1**, 011006 (2014).
- [19] A. V. Shytov, M. S. Rudner, and L. S. Levitov, Klein Backscattering and Fabry-Pérot Interference in Graphene Heterojunctions, *Phys. Rev. Lett.* **101**, 156804 (2008).
- [20] J. R. Williams, T. Low, M. S. Lundstrom, and C. M. Marcus, Gate-controlled guiding of electrons in graphene, *Nat. Nanotechnol.* **6**, 222 (2011).
- [21] M. Kim, J. H. Choi, S. H. Lee, K. Watanabe, T. Taniguchi, S. H. Jhi, and H. J. Lee, Valley-symmetry-preserved transport in ballistic graphene with gate-defined carrier guiding, *Nat. Phys.* **12**, 1022 (2016).
- [22] M. H. Liu, C. Gorini, and K. Richter, Creating and Steering Highly Directional Electron Beams in Graphene, *Phys. Rev. Lett.* **118**, 066801 (2017).
- [23] P. Brandimarte, M. Engelund, N. Papior, A. Garcia-Lekue, T. Frederiksen, and D. Sánchez-Portal, A tunable electronic beam splitter realized with crossed graphene nanoribbons, *J. Chem. Phys.* **146**, 199902 (2017).
- [24] J. Li, R. Zhang, Z. Yin, J. Zhang, and K. Watanabe, A valley valve and electron beam splitter, *Science* **362**, 1149 (2018).
- [25] A. S. Mayorov, R. V. Gorbachev, S. V. Morozov, L. Britnell, R. Jalil, L. A. Ponomarenko, P. Blake, K. S. Novoselov, K. Watanabe, T. Taniguchi, and A. K. Geim, Micrometer-scale ballistic transport in encapsulated graphene at room temperature, *Nano Lett.* **11**, 2396 (2011).
- [26] N. Yu, P. Genevet, M. Kats, F. Aieta, J. Tetienne, F. Capasso, and Z. Gaburro, Light propagation with phase discontinuities: Generalized laws of reflection and refraction, *Science* **334**, 333 (2011).
- [27] X. Ni, N. K. Emani, A. V. Kildishev, A. Boltasseva, and V. M. Shalaev, Broadband light bending with plasmonic nanoantennas, *Science* **335**, 427 (2012).
- [28] J. Du, Z. Lin, S. Chui, W. Lu, H. Li, A. Wu, Z. Sheng, J. Zi, X. Wang, S. Zou, and F. Gan, Optical Beam Steering Based on the Symmetry of Resonant Modes of Nanoparticles, *Phys. Rev. Lett.* **106**, 203903 (2011).
- [29] J. Du, Z. Lin, S. Chui, G. Dong, and W. Zhang, Nearly Total Omnidirectional Reflection by a Single Layer of Nanorods, *Phys. Rev. Lett.* **110**, 163902 (2013).
- [30] N. Yu and F. Capasso, Flat optics with designer metasurfaces, *Nat. Mater.* **13**, 139 (2014).
- [31] P. Wan, Y. Ren, Q. Wang, D. Huang, L. Zhou, H. Guo, and J. Du, Dirac fermion metagratings in graphene, *npj 2D Mater. Appl.* **5**, 42 (2021).
- [32] M. Khorasaninejad, W. T. Chen, R. C. Devlin, J. Oh, A. Y. Zhu, and F. Capasso, Metalenses at visible wavelengths: Diffraction-limited focusing and subwavelength resolution imaging, *Science* **352**, 1190 (2016).
- [33] L. Huang, X. Chen, H. Mühlenbernd, H. Zhang, S. Chen, B. Bai, Q. Tan *et al.*, Three-dimensional optical holography using a plasmonic metasurface, *Nat. Commun.* **4**, 2808 (2013).
- [34] X. Ni, A. Kildishev, and V. Shalaev, Metasurface holograms for visible light, *Nat. Commun.* **4**, 2807 (2013).
- [35] T. Cui, M. Qi, X. Wan, J. Zhao, and Q. Cheng, Coding metamaterials, digital metamaterials and programmable metamaterials, *Light Sci. Appl.* **3**, e218 (2014).
- [36] C. Liu, Q. Ma, Z. Luo, Q. Hong, Q. Xiao, H. Zhang, L. Miao *et al.*, A programmable diffractive deep neural network based on a digital-coding metasurface array, *Nat. Electron.* **5**, 113 (2022).
- [37] R. L. Heinisch, F. X. Bronold, and H. Fehske, Mie scattering analog in graphene: Lensing, particle confinement, and depletion of Klein tunneling, *Phys. Rev. B* **87**, 155409 (2013).
- [38] M. I. Katsnelson, F. Guinea, and A. K. Geim, Scattering of electrons in graphene by clusters of impurities, *Phys. Rev. B* **79**, 195426 (2009).
- [39] P. M. Ostrovsky, I. V. Gornyi, and A. D. Mirlin, Electron transport in disordered graphene, *Phys. Rev. B* **74**, 235443 (2006).
- [40] M. Hentschel and F. Guinea, Orthogonality catastrophe and Kondo effect in graphene, *Phys. Rev. B* **76**, 115407 (2007).
- [41] D. S. Novikov, Elastic scattering theory and transport in graphene, *Phys. Rev. B* **76**, 245435 (2007).
- [42] C. Schulz, R. L. Heinisch, and H. Fehske, Scattering of two-dimensional Dirac fermions on gate-defined oscillating quantum dots, *Phys. Rev. B* **91**, 045130 (2015).
- [43] J. Cserti, A. Pályi, and C. Péterfalvi, Caustics Due to a Negative Refractive Index in Circular Graphene P-N Junction, *Phys. Rev. Lett.* **99**, 246801 (2007).

- [44] A. Pieper, R. L. Heinish, and H. Fehske, Electron dynamics in graphene with gate-defined quantum dots, *Europhys. Lett.* **104**, 47010 (2013).
- [45] J. M. Caridad, S. Connaughton, C. Ott, H. B. Weber, and V. Krstić, An electrical analogy to Mie scattering, *Nat. Commun.* **7**, 12894 (2016).
- [46] K. Bai, J. Zhou, Y. Wei, J. Qiao, Y. Liu, H. Liu, H. Jiang, and L. He, Generating atomically sharp p-n junctions in graphene and testing quantum electron optics on the nanoscale, *Phys. Rev. B* **97**, 045413 (2018).
- [47] C. Gutiérrez, L. Brown, C.-J. Kim, J. Park, and A. N. Pasupathy, Klein tunnelling and electron trapping in nanometre-scale graphene quantum dots, *Nat. Phys.* **12**, 1069 (2016).
- [48] J. Qiao, H. Jiang, H. Liu, H. Yang, N. Yang, K. Qiao, and L. He, Bound states in nanoscale graphene quantum dots in a continuous graphene sheet, *Phys. Rev. B* **95**, 081409(R) (2017).
- [49] J. Lee, D. Wong, J. Rodriguez-Nieva, J. F. Kahn, S. Kaln, H. Tsai, T. Taniguchi *et al.*, Imaging electrostatically confined Dirac fermions in graphene quantum dots, *Nat. Phys.* **12**, 1032 (2016).
- [50] Y. Ren, Y. Gao, P. Wan, Q. Wang, D. Hunag, and J. Du, Effective medium theory for electron waves in a gate-defined quantum dot array in graphene, *Phys. Rev. B* **100**, 045422 (2019).
- [51] Y. Tang, X. Cao, R. Guo, Y. Zhang, Z. Y. Che, F. Yannick, W. Zhang, and J. Du, Flat-Lens Focusing of Electron Beams in Graphene, *Sci. Rep.* **6**, 33522 (2016).
- [52] See Supplemental Material at <http://link.aps.org/supplemental/10.1103/PhysRevB.107.155404> where we present the following: (i) an explanation for the deviation between θ_{calc} and θ_{actu} at $m_{\text{unit}} = 5$, and (ii) the near-zero reflection probability in the metasurfaces.
- [53] A. Ghaffarkhah, E. Hosseini, M. Kamkar, A. A. Sehat, S. Dordanihaghighi, A. Allahbakhsh, C. van der Kuur, and M. Arjmand, Synthesis, applications, and prospects of graphene quantum dots: A comprehensive review, *Small* **18**, 2102683 (2022).
- [54] J. Koringa, On the calculation of the energy of a Bloch wave in a metal, *Physica* **13**, 392 (1947).
- [55] W. Kohn and N. Rostoker, Solution of the Schrodinger equation in periodic lattices with an application to metallic lithium, *Phys. Rev.* **94**, 1111 (1954).